**ORIGINAL ARTICLE**

# Enhanced Performance of Electrical Double-Layer Capacitor by Controlling the Specific Surface Area and Pore Structure of ZIF-67

U Hyeok Son[1] · Seon Yeong Lee[1] · Han-Ik Joh[1]

## Abstract

Electrical double-layer capacitance can be enhanced by developing carbon materials with elevated specific surface area, porosity, and electrical conductivity. In this study, we demonstrate a facile approach for synthesizing carbon materials with a meticulously controlled pore structure of ZIF-67 by a precise manipulation of the precursor solution quantities. The concentration of the precursor solution affected the crystal size of ZIF-67 due to the different nucleation rates. After the carbonization of the crystals, smaller cobalt nanoparticles were formed within the carbon materials derived from the larger ZIF-67 crystal. The removal of the nanoparticles by acid treatment induced the formation of porous carbon, resulting in the enhanced performance of the electrical double-layer capacitors. The nanoporous carbon derived from the largest-sized ZIF-67 template exhibited a remarkable specific capacitance of 157 F/g at a current density of 1 A/g, retaining an impressive 85% of this value after 30,000 charging/discharging cycles at 16 A/g.

**Keywords** Metal–organic frameworks · ZIF-67 · Nanoporous carbon · Electric double layer capacitors

## Introduction

Carbon materials have been widely used as electrodes [1–3], catalytic supports [4–6] and adsorbates [7, 8] because of their remarkable and tunable properties in both electrical and morphological aspects. In addition, the features and dimensions of carbon materials can be easily controlled by synthetic methods and raw materials. However, post-treatments, such as heteroatom doping, and activation, are required to improve the properties of bare carbon materials to make them suitable for any particular application. To date, many approaches have been utilized to develop carbon materials with improved characteristics [9–11]. Gandla et al. designed mesoporous-activated carbon with nitrogen (N) atoms from a biomass material, which was carbonized and followed by N-doping with melamine [12]. They demonstrated that an optimum content of N atoms and high mesoporosity increased the conductivity and specific capacitance of the material.

In addition, Cheng et al. combined activated carbon with 1-dimensional carbon materials, such as carbon nanotubes (CNTs) and carbon nanofibers (CNFs), through a simple slurry process to develop multi-component nanocomposites [13]. Owing to the synergistic effect of the multidimensional nanocomposites, the electrodes exhibited remarkable performance compared to mono/binary component electrodes. Reduced graphene oxide (rGO) with 2-dimensional features has been extensively studied as an electrochemical material [14–17]. rGO was synthesized by the exfoliation of graphite and reduction of graphene oxide, resulting in more defects and lower quality than graphene. However, the electronic and morphological properties of the rGO can be easily modified by heteroatom doping and post-treatment [18, 19]. Li et al. proposed a strategy for preparing highly capacitive rGO papers using Zn powder that can be completed within an hour [20]. Several other synthetic approaches, such as template method and carbonization-activation methods, have also been applied to develop conventional carbon materials with better properties [21]. However, these restacked materials inherently require additional steps to control their pore structure, which significantly affects the performance of electric double-layer capacitors (EDLCs).

Recently, metal–organic frameworks (MOFs) gained attention in various fields, such as catalysis, gas adsorption,

✉ Han-Ik Joh
hijoh@konkuk.re.kr

1 Department of Energy Engineering, Konkuk University, 120 Neungdong-ro, Gwangjin-gu, Seoul 05029, Republic of Korea

and separation [22–24], because of their precisely controlled pore structure and surface morphologies. Carbon materials derived from MOFs exhibit large specific surface areas, highly ordered structures, and porous morphologies owing to their original properties. Zeolitic imidazolate frameworks (ZIFs) are subclass of MOFs, consisting of tetrahedral metal (Co, Zn, Cu, etc.) atoms in the center bonded to imidazole ligands. The bonding angle between the metal cation and the ligand is ~ 145°, which is similar to that of conventional zeolites. In particular, ZIF-67, which consists of Co cations and 2-methyl imidazolate anions, has a high surface area, micropores, and a cubic crystal symmetric structure [25], leading to its wide application in catalysis, drug delivery, and supercapacitors. Moreover, carbon materials derived from ZIF-67 can additionally exhibit high electrical conductivity and electrochemical stability owing to the catalytic graphitization of Co particles. Interestingly, numerous studies have demonstrated that porous carbon materials derived from ZIF-67 alone, composite materials of ZIF-67, and other ZIFs exhibit remarkable specific capacitances. Torad et al. reported that porous carbon from ZIF-67 showed a value of 238 F/g in 0.5 M $H_2SO_4$ [26]. Tang et al. prepared core–shell ZIF composites, consisting of Zn-based ZIF (ZIF-8) and ZIF-67 as the core and shell, respectively [27]. They suggested that the ZIF-8-derived carbon core had a large specific surface area and high N content, whereas the ZIF-67-derived carbon shell exhibited high electrical conductivity. The optimum molar ratio of $Co^{2+}/Zn^{2+}$ was 0.05, at which the surface area, porosity, and N content were higher than those of the ZIF-8-derived carbon, leading to improved electrochemical performance.

In this study, we investigated the size effect of ZIF-67 crystals on the electrochemical capacitances by controlling the amount of the precursor solution. The crystal size was varied in the range from 500 nm to 1 μm. Interestingly, the specific surface areas and porosities of carbonized and acid-treated samples increased with the increasing crystal size. The carbon material derived from the largest-sized ZIF-67 exhibited remarkable performance compared to carbon from other-sized ZIF-67. Therefore, we conclude that the crystal size of ZIF-67 affects the pore structure of carbon materials, leading to the formation of highly capacitive materials.

# Experimental

## Synthesis of ZIF-67–*x*–*y*

Cobalt nitrate hexahydrate(3 g) was dissolved in *x* mL methanol (*x* = 100, 200, and 300 mL). Next, 6 g of 2-methylimidazole was dissolved in y mL methanol (*y* = 200, 400, and 600 mL). The two solutions were then mixed under stirring for 24 h at room temperature. The purple precipitate was

separated by centrifugation (8000 rpm) and washed several times with methanol and ethanol. Finally, the purple powder, ZIF-67–*x*–*y*, where *x* represents the amount of methanol in cobalt nitrate hexahydrate solution, and *y* represents the amount of methanol in 2-methylimidazole solution was obtained after drying under vacuum at 60 °C overnight.

## Synthesis of a-CoNC–*x*–*y*

ZIF-67–*x*–*y* was carbonized in the flowing Ar at 800 °C for 1 h. The heating mantle was rapidly removed for cooling. After cooling to room temperature, the obtained black powder was sonicated in 0.5 M $_2SO_4$ for 2 h and aged at room temperature for 18 h to remove excess Co species. Finally, a-CoNC–*x*–*y* was obtained after washing repetitively with deionized $H_2O$ and vacuum drying at 80 °C. For comparison, CoNC-*x*–*y* was also analyzed without acid washing to demonstrate the effect of Co metal removal.

## Characterization

The crystal sizes and morphologies of ZIF-67–*x*–*y* and a-CoNC-*x*–*y* were characterized using field-emission scanning electron microscopy (FE-SEM, SU8010, Hitachi High-Tech, Japan). X-ray diffraction (XRD) patterns were collected on a Rigaku diffractometer with Cu Kα radiation. Transmission electron microscopy (TEM) images were obtained using a JEM-2010 microscope (JEOL, Japan). X-ray photoelectron spectroscopy (XPS) measurements were conducted by a Thermo Scientific Kα system. The specific surface area and porosity were measured using the Brunauer–Emmett–Teller (BET) method on a Micromeritics ASAP 2460 instrument (Micromeritics Instrument Corp., USA) at liquid-nitrogen temperature.

## Electrochemical Analysis

All electrochemical measurements were performed using an Autolab PGSTAT 302N potentiostat (Metrohm Autolab, Netherlands) with a three-electrode system in 1 M KOH solution. A Pt wire, Ag/AgCl, and glassy carbon electrode ($\Phi$ = 5 mm) were used as the counter electrode, reference electrode, and working electrode, respectively. For preparation of the working electrode, 5 mg of as-synthesized materials, 150 μL of deionized $H_2O$, 350 μL of ethanol, and 50 *uL* of Nafion (Sigma Aldrich, USA) were sonicated for 30 min. The slurry was dropped onto glassy carbon to meet a loading amount of 0.370 mg/cm$^2$.

The electrochemical properties of the working electrode were investigated using cyclic voltammetry (CV), galvanostatic charge–discharge measurements (GCD), and electrochemical impedance spectrum (EIS) measurements. The specific capacitance (F/g) was calculated from the CV

curves using the following equation: $C = \frac{\int_{V_i}^{V_f} I(V)\mathrm{d}V}{mv(V_f - V_i)}$, where m is the mass loading of the active material (0.370 mg/cm$^2$), $v$ is the potential scan rate, $V_f$ and $V_i$ are the investigated potential limits, and $I(V)$ is the current density. The specific capacitance was also calculated from the GCD curves using the following equation: $C = \frac{I \times \Delta t}{m \times \Delta V}$, where $I$ is the charge–discharge current at a discharge time $\Delta t$(s), m is the mass loading amount of active material, and $\Delta V$ is the potential window.

## Results and Discussion

ZIF-67 particles of various crystal sizes were synthesized as a function of the amount of methanol in the precursor solutions. The XRD patterns of our samples perfectly matched the simulated XRD peaks of ZIF-67 (JCPDS: 00-062-1030), indicating that ZIF-67 s were successfully synthesized regardless of the concentration of precursor solutions (Fig. 1a). The morphology and crystal size of the ZIF-67s were verified through FE-SEM images (Fig. 1b–d). All samples exhibited rhombic dodecahedral structures with different crystal sizes. The average crystal sizes were $525.8 \pm 96$ nm, $620.3 \pm 127$ nm, and $1140.7 \pm 248$ nm for ZIF-67–100–200, ZIF-67–200–400, and ZIF-67–300–600,

respectively. That is, as the amount of methanol increased, the crystal size increased. This is a well-known crystal growth mechanism in which atoms start to form nuclei above a certain concentration of atoms, and then the nuclei keep growing because of the additional atoms, leading to the formation of the crystal [28, 29]. Considering the general mechanism, the number of ZIF-67 nuclei may increase when the precursor concentrations are high. That is, in the case of a high precursor concentration, the precursor might mainly participate in the nuclei formation reaction rather than in the crystal growth reaction, leading to the formation of small crystals. Hence, we observed the formation of small crystals from low methanol content.

ZIF-67 crystals can be transformed into Co- and N-doped carbon materials (CoNC) through a facile carbonization. Figure S1a–c show that our samples maintained the original morphology of ZIF-67, even though there was a reduction in size and a rougher surface. The average crystal sizes decreased to $320.8 \pm 81$ nm, $444.9 \pm 87$ nm, and $795.7 \pm 161$ nm for CoNC-100–200, CoNC-200–400, and CoNC-300–600, respectively. During carbonization, the cobalt ions coordinated with nitrogen atoms underwent reduction to form cobalt nanoparticles, which tended to aggregate and form larger cobalt nanoparticles. These nanoparticles acted as catalysts for graphitization during the carbonization [30], thus enhancing the electrical conductivity of
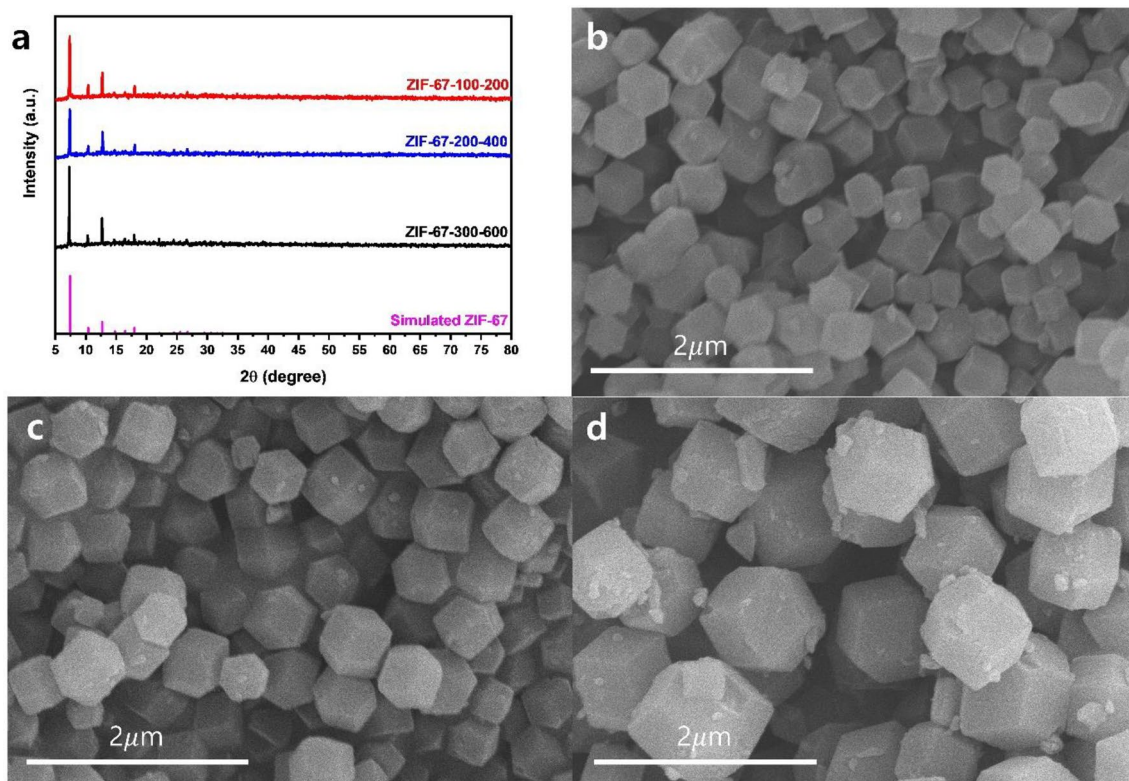


**Fig. 1** **a** XRD patterns of ZIF-67s **b–d** FE-SEM images of ZIF-67s (**b** ZIF-67–100–200, **c** ZIF-67–200–400, **d** ZIF-67–300–600)

the CoNCs. In Figure S2a, XRD patterns of CoNC-*x*–*y* are presented. The broad peak around 2θ of 26° was attributed to the (002) plane of carbon, while the (111) and (200) diffractions of the face-centered cubic (fcc) Co were observed at 44.2° and 51.5°, respectively. The size of the cobalt nanoparticles exhibited about 17.8 nm, 14.9 nm, and 14.0 nm for CoNC-100–200, CoNC-200–400, and CoNC-300–600, respectively, as calculated using the Scherrer equation.

To increase the gravimetric energy density of the carbon materials, Co nanoparticles should be removed, even though they help to improve the crystallinity of the materials. The nanoparticles were acid-leached out by 0.5 M $H_2SO_4$, which is a mildly acidic condition due to the suppression of structural deactivation of the carbon materials. Interestingly, the morphological features of the acid-treated CoNC-*x*–*y* (a-CoNC-*x*–*y*) samples were maintained, even though the Co nanoparticles embedded in the CoNC structure were leached out, as shown in Fig. 2a–c. However, the diffraction peak at around 26° became more pronounced, indicating the removal of amorphous carbon during the acid treatment, as depicted in Figure S2b. The TEM images confirmed the presence of a graphitic structure and voids in the a-CoNCs. Relatively small Co nanoparticles (about 1–2 nm) were eliminated after the acid treatment, while larger Co nanoparticles (about 7–20 nm) were reduced in size, regardless of the crystal size of the CoNCs. In addition, many voids originated from the elimination of nanoparticles were observed, as shown in Fig. 2d–f. Hence, we believe that the a-CoNC particles have two incompatible properties: porosity and crystallinity.

To assess the porosity of the synthesized ZIF-67 s and CoNCs, we conducted $N_2$ gas adsorption–desorption experiments at liquid nitrogen temperature. Despite variations in the crystal sizes of ZIF-67 s, the BET surface areas were consistently measured between 1400 and 1450 $m^2$/g. The isotherms of ZIF-67s exhibited a type-I behavior (Fig. 3a), indicating their predominantly microporous nature. Pore size distribution (PSD) analysis using Density Functional Theory (DFT) revealed dominant micropores with widths of 1.00 nm and 1.48 nm, with no mesopores detected (Fig. 3b). In contrast, both CoNCs and a-CoNCs exhibited type-IV isotherms with hysteresis loops, as shown in Fig. 3c and d, respectively, indicating the coexistence of micropores and mesopores. Notably, the hysteresis loop in the a-CoNCs was more pronounced, indicating the formation of mesopores after acid treatment. To further characterize the pore structures of CoNCs and a-CoNCs, we quantified the micro- and mesopore volumes using DFT (Table S1). The BET surface area and micro- /mesopore volume exhibited slight increases with increasing crystal sizes of CoNCs. However, a substantial enhancement in the surface area and porosity was observed after the acid treatment, which was attributed to the removal of cobalt species and amorphous carbon. Particularly noteworthy is the increase in the surface area and pore volume, which are highly related to the crystal size. In our previous work, we found that zinc nanoparticles in relatively larger ZIF-8 were more efficiently removed than those in small-sized ZIF-8 [31]. Thus, it can be concluded that the more efficient removal of cobalt nanoparticles from larger
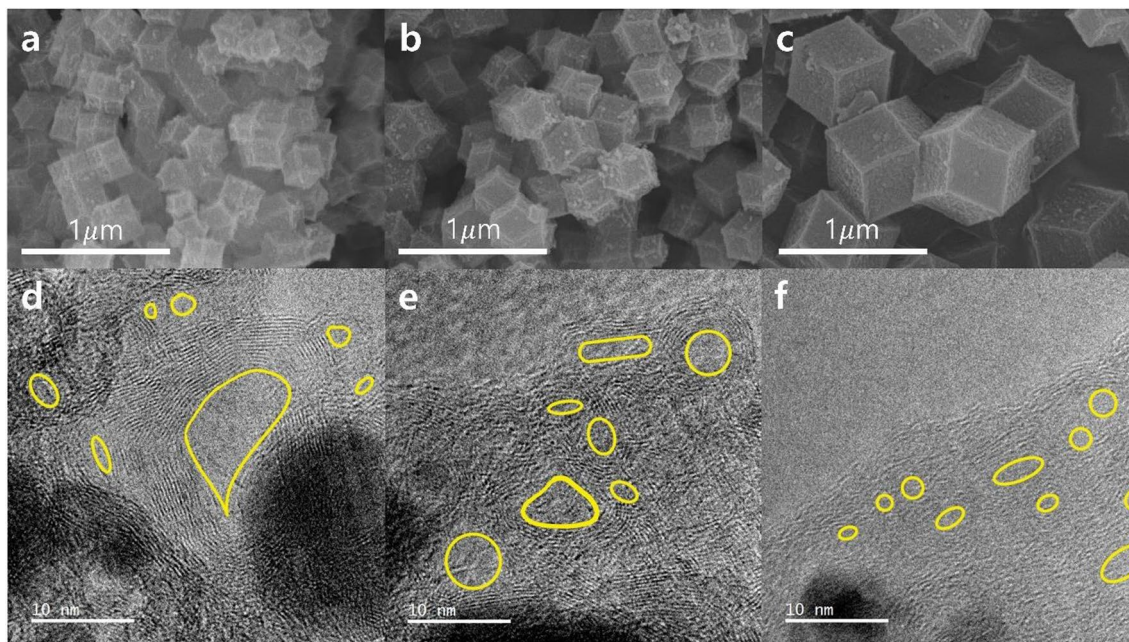


**Fig. 2** FE-SEM images of a-CoNCs **a** a-CoNC-100–200, **b** a-CoNC-200–400, **c** a-CoNC-300–600 and TEM images of **d** a-CoNC-100–200, **e** a-CoNC-200–400, and **f** a-CoNC-300–600. The yellow marks represent the voids formed by acid treatment
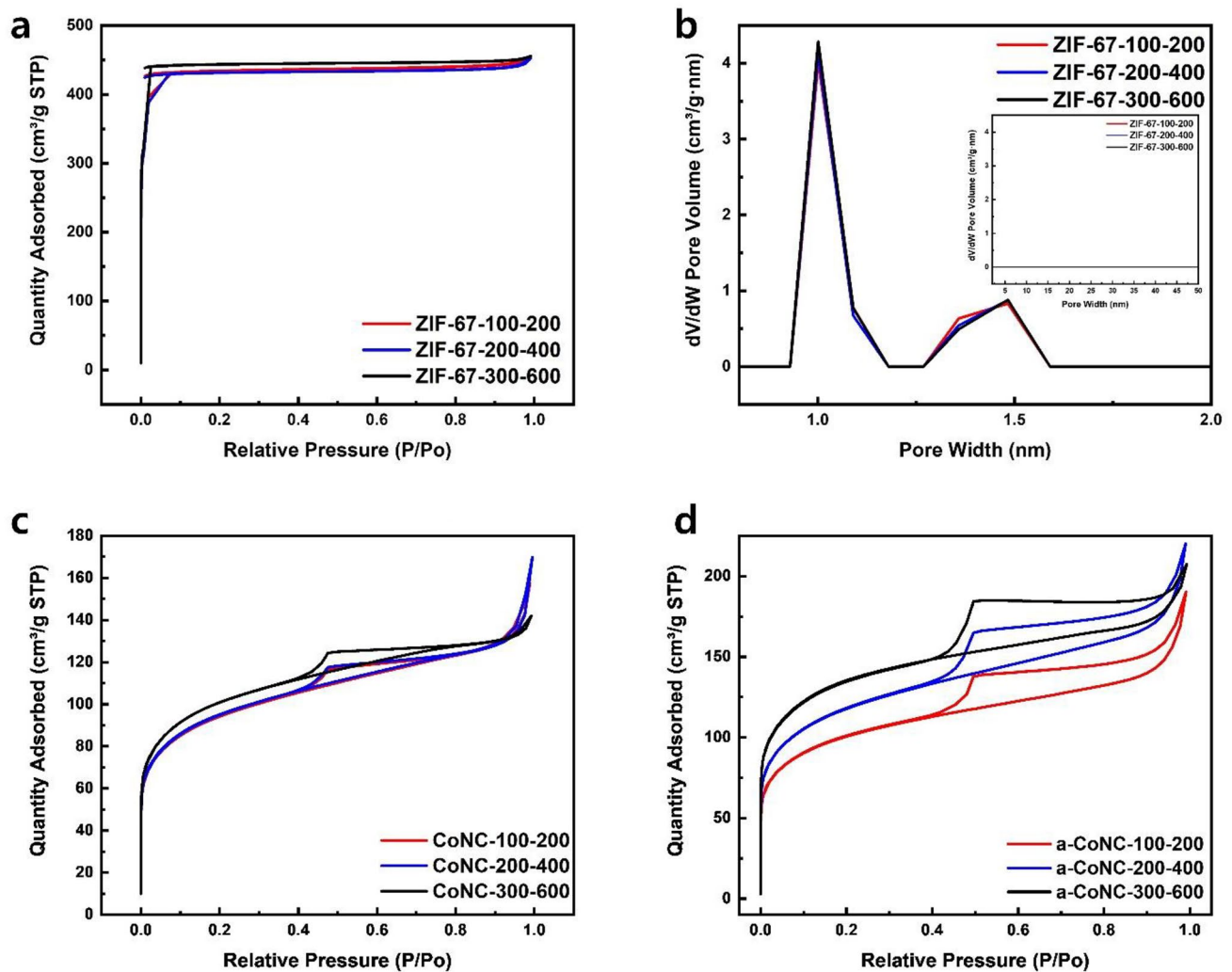
**Fig. 3** **a** $N_2$ adsorption–desorption isotherms, **b** DFT pore size distribution of ZIF-67s (inset is the PSD in the range of mesopores), and $N_2$ adsorption–desorption isotherms of **c** CoNCs, and **d** a-CoNCs

CoNCs affects the formation of micro- and mesoporous carbon.

The chemical configurations of the CoNCs and a-CoNCs were investigated using X-ray photoelectron spectroscopy (XPS) as illustrated in Figures S3 and 4, respectively. The wide-scan spectrum reveals the presence of four elements: C, N, Co, and O. The deconvolution of the C 1s spectrum identified various carbon species: C=C (284.1 eV), C–C (284.75 eV), C–O–H (285.5 eV), C–N and C–O–C (286.3 eV), C=O (288.5 eV), O=C–O (289.47 eV), and $\pi–\pi^*$ (291.04 eV) as shown in Fig. 4b. The quantification of each deconvoluted C 1s peak is summarized in Table S2, confirming the high carbon contents, particularly sp2-bonded carbon, in CoNC-300–600 and a-CoNC-300–600. This might have originated from the size of ZIF-67 because gaseous carbon species in relatively larger particles are more challenging to evolve, resulting in an increase in the carbon

content of the carbonized particles. The N 1s spectrum was deconvoluted into six peaks: pyridinic-N (398.5 eV), Co–N (399.42 eV), pyrrolic-N (400.5 eV), graphitic-N (401.3 eV), N–O (402.8 eV), and N-Ox (405 eV) as shown in Fig. 4c. Nitrogen atoms of approximately 8 at% were incorporated into our samples, even though there are negligible variations between CoNCs and a-CoNCs. It is well known that nitrogen atoms with lone pair electrons enhance the partial density of electrons in carbon materials, leading to an improvement in the charge transfer resistance [32]. Partially removed Co metal was also detected, as shown in Fig. 4d. The Co 2p spectrum exhibited four major peaks: $Co^0$ (778.4 eV), $Co^{3+}$ (779.7 eV), $Co^{2+}$ (780.9 eV), and Co satellite (784.5 eV). Interestingly, as the crystal size of the a-CoNCs increased, the total amount of metallic Co decreased. Moreover, the reduction in cobalt species was more pronounced in the a-CoNCs with larger crystal sizes than in the CoNCs. This
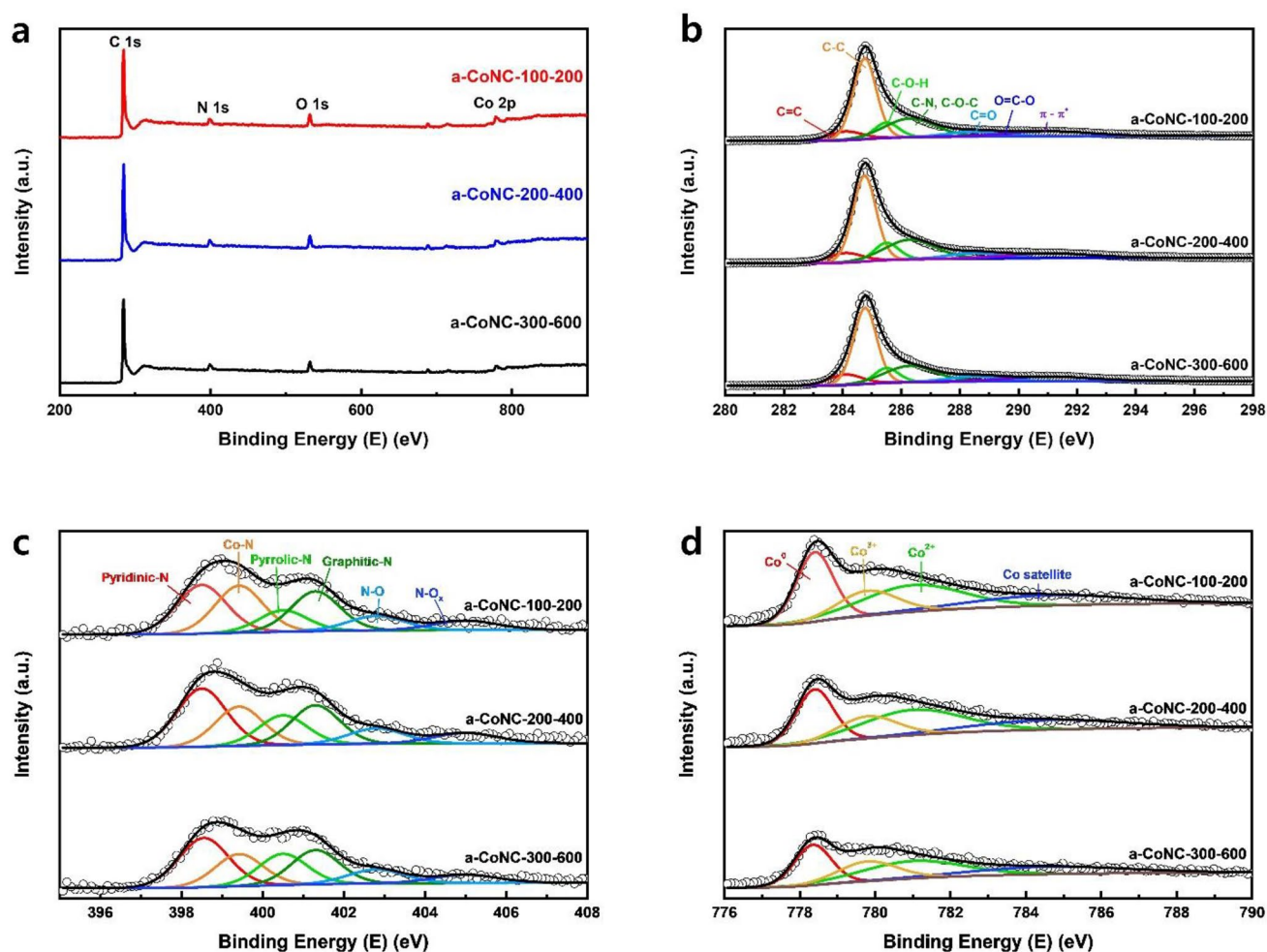
**Fig. 4** XPS spectrum of a-CoNCs **a** wide scan survey **b** C 1s, **c** N 1s, and **d** Co 2p

suggests that the smaller cobalt nanoparticles were more readily eliminated, as supported by the XRD and TEM results.

To evaluate the electrochemical properties of CoNCs, we conducted cyclic voltammetry (CV) and galvanostatic charge–discharge (GCD) measurements using a three-electrode system in a 1.0 M KOH aqueous electrolyte (Fig. 5). Cyclic voltammograms were recorded at various scan rates ranging from 40 to 200 mV/s (Figure S4). All CV curves exhibited rectangular shapes, indicative of the non-Faradaic reactions characteristic of electrical double-layer capacitors (EDLCs). The specific capacitances of the a-CoNCs, calculated from the data in Fig. 5a, were determined to be 114, 126, and 145 F/g for a-CoNC-100–200, a-CoNC-200–400, and a-CoNC-300–600, respectively. The superior electrochemical performance of a-CoNC-300–600 may be attributed to its high specific surface area and significant micro-mesopore volume, which originated from its larger crystal size.

To further investigate the impact of carbonization and acid treatment, we conducted specific capacitance measurements for both ZIF-67s and CoNCs (Figure S5). Despite ZIF-67s exhibiting a high specific surface area, their capacitance values remained below 2 F/g owing to their micropores and low electrical conductivity. Interestingly, in the case of CoNCs, their capacitive behaviors exhibited similarity and the specific capacitance values for CoNC-100–200, CoNC-200–400, and CoNC-300–600 were approximately 78, 84, and 82 F/g, respectively. As expected from the $N_2$ physisorption results, the analogous electrochemical capacitive values of the CoNCs are attributed to their comparable morphological characteristics. Furthermore, the removal of Co nanoparticles can stimulate the generation of micro- and mesopores, consequently enhancing the capacitance of a-CoNCs compared to that of CoNCs.

GCD measurements were conducted at current densities ranging from 1to 16 A/g (Fig. 5b–f). Linear discharge profiles of non-Faradaic reactions were observed for all
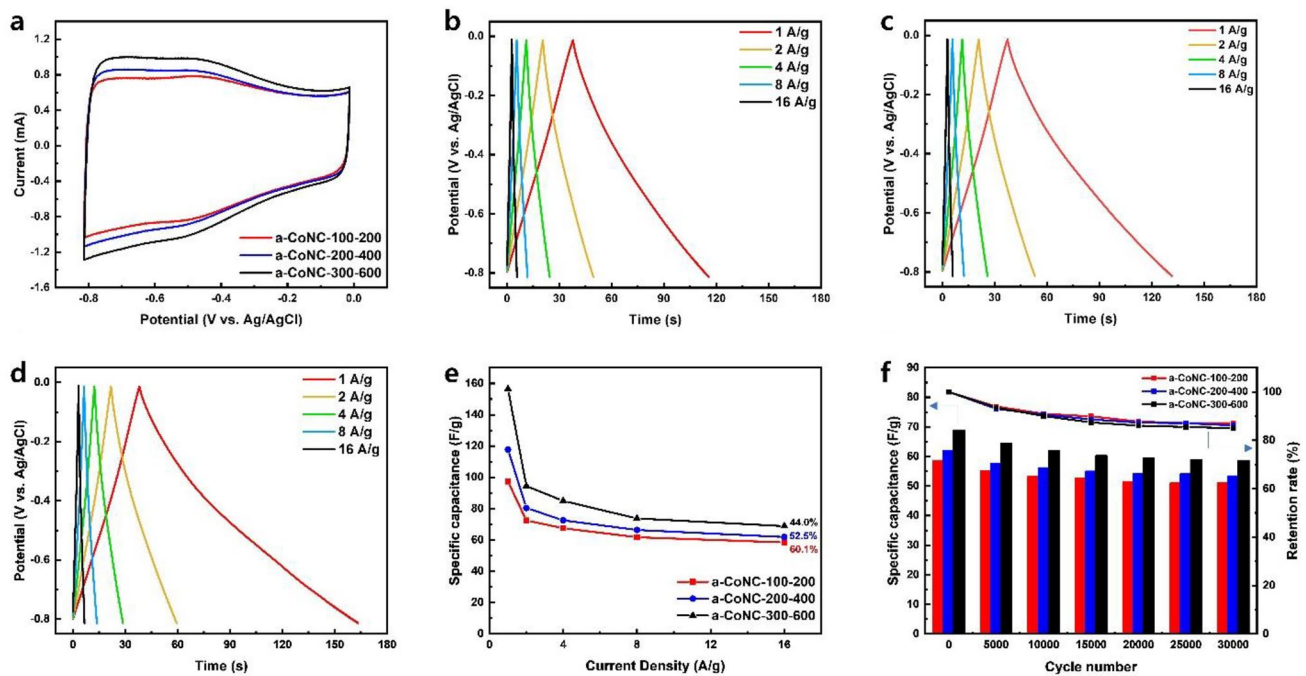
**Fig. 5** **a** CV curves at a scan rate of 200 mV/s, GCD curves at different current densities for **b** a-CoNC-100–200, **c** a-CoNC-200–400, **d** a-CoNC-300–600, **e** specific capacitance as a function of current density, and **f** Cyclic stability at a charge/discharge current density of 16 A/g for 30,000 cycles of a-CoNCs

a-CoNCs, indicating the typical behavior of EDLCs. The specific capacitances calculated at the current density of 1 A/g were 97, 118, and 157 F/g for a-CoNC-100–200, a-CoNC-200–400, and a-CoNC-300–600, respectively. At the high current density of 16 A/g, the retention rates were 60.1%, 52.5%, and 44.0% for a-CoNC-100–200, a-CoNC-200–400, and a-CoNC-300–600, respectively (Fig. 5e). Considering charge transport in porous materials, the lower retention rate of CoNC-300–600 might be attributed to its higher micropore volume. At low current densities, both external and internal pores can act as active surfaces, while at high current densities, the diffusion of electrolyte ions into the micropores becomes restricted. Despite having lowest retention rate, a-CoNC-300–600 exhibited the highest specific capacitance of 69 F/g at the highest rate of 16 A/g, surpassing that of a-CoNC-100–200 (58 F/g) and a-CoNC-200–400 (62 F/g). The cycle stability was evaluated through 30,000 charge–discharge cycles at 16 A/g. Remarkably, all the a-CoNCs retained approximately 85% of their initial capacitance (Fig. 5f). This robust stability can be attributed to the stable and well-ordered structure of the CoNCs catalyzed by the Co nanoparticles and the high content of N atoms with lone-pair electrons.

## Conclusion

Various crystal sizes of ZIF-67s were synthesized by modulating the nucleation rate, which was achieved through a precise control of the precursor solution quantities. Through following carbonization and acid treatment, we observed notable increases in the specific surface area and porosity, as well as in the contents of sp2-carbon and N-doped carbon, corresponding to the enlargement of the ZIF-67 crystal sizes. The largest a-CoNC was characterized by a specific surface area of 483.3 $m^2$/g and an sp2-carbon content of 7.6 at%, whereas the specific surface area was 357.8 $m^2$/g and had 5.9 at% of sp$^2$-carbon in the smallest-sized a-CoNC. Consequently, variations in the ZIF-67 crystal size yielded remarkable differences in the electrochemical performance, resulting in the highest specific capacitance of 157 F/g achieved by the largest a-CoNC. Hence, we believe that our approach presents a straightforward method for improving the performance of EDLCs, with potential applicability to other materials based on ZIF-67.

**Data availability** All data presented in this study are available from the corresponding authors (H.-I. Joh) upon request.

# References

1. S. Yuan, Q. Lai, X. Duan, Q. Wang, J. Energy Storage **61**, 106716 (2023)
2. L. Deng, T. Wei, J. Liu, L. Zhan, W. Chen, J. Cao, Crystals **12**, 1279 (2022)
3. S.H. Kwon, E. Lee, B.-S. Kim, S.-G. Kim, B.-J. Lee, M.-S. Kim, J.C. Jung, Korean J. Chem. Eng. **14**, 603 (2014)
4. E. Lam, J.H.T. Luong, ACS Catal. **4**, 3393–3410 (2014)
5. A.A. Stepacheva, M.E. Markova, Y.V. Lugovoy, YYu. Kosivtsov, V.G. Matveeva, M.G. Sulman, Catalysts **13**, 655 (2023)
6. D. Zhang, G. Wei, Y. Wang, J. Wang, P. Ning, Q. Zhang, M. Wang, T. Zhang, K. Long, Korean J. Chem. Eng. **35**, 1979 (2018)
7. M.M. Sabzehmeidani, S. Mahnaee, M. Ghaedi, H. Heidari, V.A.L. Roy, Mater. Adv. **2**, 598–627 (2021)
8. S. Khalili, M. Jahanshahi, Korean J. Chem. Eng. **38**(4), 862–871 (2021)
9. S.-H. Yoon, S. Lim, Y. Song, Y. Ota, W. Qiao, A. Tanaka, I. Mochida, Carbon **42**, 1723–1729 (2004)
10. C.H. Kwak, C. Lim, S. Kim, Y.-S. Lee, J. Ind. Eng. Chem. **116**, 21–31 (2022)
11. K.D. Stephane, M. Gupta, A. Kumar, V. Sharma, S. Pandit, P. Bocchetta, Y. Kumar, J. Compos. Sci. **5**, 66 (2021)
12. D. Gandla, X. Wu, F. Zhang, C. Wu, D.Q. Tan, ACS Omega **6**, 7615–7625 (2021)
13. F. Cheng, X. Yang, S. Zhang, W. Lu, J. Power. Sources **450**, 227678 (2020)
14. L. Yang, L. Zhang, X. Jiao, Y. Qiu, W. Xu, RSC Adv. **11**, 4042–4052 (2021)
15. S. Choi, C. Kim, J.M. Suh, H.W. Jang, Carbon Energy **1**, 85–108 (2019)
16. S.B. Patil, B. Kishore, G. Nagaraju, J. Dupont, N. J. Chem. **42**, 18569–18577 (2018)
17. S.Y. Hwang, C.-H. Lee, H.R. Lee, S.-Y. Son, S. Lee, H.-I. Joh, Chem. Eng. Sci. **231**, 116301 (2021)
18. Z. Di, H. Shen, Y. Guo, X. Guo, B. Kang, M. Guo, Y. Wei, J. Jia, R. Zhang, Chem. Phys. Impact **5**, 100103 (2022)
19. S. Mullner, T. Held, T. Tichter, P. Rank, D. Leykam, W. Jiang, T. Lunkenbein, T. Gerdes, C. Roth, J. Electrochem. Soc. **170**, 070523 (2023)
20. Y.-F. Li, Y.-Z. Liu, W.-K. Zhang, C.-Y. Guo, C.-M. Chen, Mater. Lett. **157**, 273–276 (2015)
21. J. Yin, W. Zhang, N.A. Alhebshi, N. Salah, H.N. Alshareef, Small Methods **4**, 1900853 (2020)
22. S.Y. Lee, J.Y. Lee, H.-W. Jang, U.H. Son, S. Lee, H.-I. Joh, J. Ind. Eng. Chem. **117**, 434–441 (2023)
23. V. Pirouzfar, N. Roustaie, C.-H. Su, Korean J. Chem. Eng. **40**(9), 2138–2148 (2023)
24. H.-W. Jang, S.Y. Lee, J.Y. Lee, H.-I. Joh, Carbon Lett. **33**, 215–223 (2023)
25. C. Duan, Y. Yu, H. Hu, Green Energy Environ. **7**, 3–15 (2022)
26. N.L. Torad, R.R. Salunkhe, Y. Li, H. Hamoudi, M. Imura, Y. Sakka, C.-C. Hu, Y. Yamauchi, Chem. Eur. J. **20**, 7895–7900 (2014)
27. J. Tang, R.R. Salunkhe, J. Liu, N.L. Torad, M. Imura, S. Furukawa, Y. Yamauchi, J. Am. Chem. Soc. **137**, 1572–1580 (2015)
28. K.A.S. Usman, J.W. Maina, S. Seyedin, M.T. Conato, L.M. Payawan Jr., L.F. Dumee, J.M. Razal, NPG Asia **12**, 58 (2020)
29. J.J. Beh, J.K. Lim, E.P. Ng, B.S. Ooi, Mater. Chem. Phys. **216**, 393–401 (2018)
30. S.J. Goldie, S. Jiang, K.S. Coleman, Mater. Adv. **2**, 3353 (2021)
31. H.-W. Jang, G.-S. Kang, J.Y. Lee, S.Y. Lee, G. Lee, S.J. Yoo, S. Lee, H.-I. Joh, Chem. Eng. J. **474**, 145464 (2023)
32. Y. Liu, H. Yu, C. Shi, Z. Xiang, J. Mater. Chem. A **9**, 19625–19630 (2021)